Internal consistency of multi-tier GW+EDMFT

Check for updates

Ruslan Mushkaev [1] ✉, **Francesco Petocchi**[2], **Viktor Christiansson**[1] **& Philipp Werner**[1]

The multi-tier GW+EDMFT scheme is an ab-initio method for calculating the electronic structure of correlated materials. While the approach is free from ad-hoc parameters, it requires a selection of appropriate energy windows for describing low-energy and strongly correlated physics. In this study, we test the consistency of the multi-tier description by considering different low-energy windows for a series of cubic SrXO$_3$ (X = V, Cr, Mn) perovskites. Specifically, we compare the 3-orbital t_{2g} model, the 5-orbital $t_{2g} + e_g$ model, the 12-orbital $t_{2g} + O_p$ model, and (in the case of SrVO$_3$) the 14-orbital $t_{2g} + e_g + O_p$ model and compare the results to available photoemission and X-ray absorption measurements. The multi-tier method yields consistent results for the t_{2g} and $t_{2g} + e_g$ low-energy windows, while the models with O_p states produce stronger correlation effects and mostly agree well with experiment, especially in the unoccupied part of the spectrum. We also discuss the consistency between the fermionic and bosonic spectral functions and the physical origin of satellite features, and present momentum-resolved charge susceptibilities.

Materials with strong electron-electron interactions exhibit diverse and remarkable properties such as high-T_c superconductivity, colossal magnetoresistance, and interaction-driven metal-insulator transitions, and are thus of central interest in condensed matter physics[1]. A widely studied subclass of these materials is the transition metal oxides, which contain partially filled narrow d-electron bands. These give rise to strong correlation phenomena, which cannot be captured at the level of effective single-particle descriptions. Theoretical studies of transition metal oxides often involve a combination of Density Functional Theory (DFT)[2,3] in the Local Density Approximation (LDA)[3] and Dynamical Mean Field Theory (DMFT)[4]. The combined DFT + DMFT scheme has been successful in reproducing a wide range of correlated electron phenomena, including mass enhancements[5], and localized to itinerant electronic transitions[6]. This approach however suffers from two main drawbacks: the reliance on ad-hoc parameters such as Hubbard U and Hund's J interactions, and the double counting of interaction energies[7]. DFT + DMFT hence cannot be considered a truly ab-initio method, and more sophisticated approaches need to be developed for reliable first-principles predictions of the properties of correlated materials.

A promising way forward is the GW + Extended Dynamical Mean Field Theory (EDMFT)[8–11] method which is based on the GW formalism[12] and supplements the nonlocal GW self-energy and polarization with more accurate estimates of the local components calculated by EDMFT. Since both GW and EDMFT are diagrammatic methods, a double counting of self-energy and polarization contributions can be easily avoided. A further advantage of the GW+EDMFT formalism is that it involves no ad-hoc

interaction parameters since these are computed self-consistently, making it a genuinely ab-initio method. In the multi-tier implementation of the framework[9,10], different degrees of freedom are treated at an appropriately chosen level of approximation. The full band space (TIER III) is treated at the level of one-shot GW (G^0W^0), while the physically more relevant low-energy subspace around the Fermi level (TIER II) is solved with the fully self-consistent $GW + EDMFT$ scheme. In this self-consistency loop, due to the complexity of the many-body problem, only the local correlations of the most strongly correlated orbitals (TIER I) are treated with EDMFT.

If the downfolding from the higher-energy to the lower-energy subspaces was implemented exactly, and we could exactly solve the resulting many-body problem, then the low-energy correlated electronic structure would be independent of the choice of energy windows.

In reality, approximations are made, both in the downfolding[13] and in the solution of the low-energy effective theory (e. g. density-density approximation in the impurity interaction), and it is thus important to understand how much the low-energy physics depends on the choice of the different tiers in the multi-tier approach. In this study, we systematically test the internal consistency of our GW+EDMFT scheme using the well-characterized and studied family of correlated perovskite compounds SrXO$_3$ (X = V, Cr, Mn) as our test materials. Specifically, we will compare the 3-band (t_{2g}) description to the five-band ($t_{2g} + e_g$) modeling and to a 12-band treatment, which in addition to the t_{2g} states also includes the Oxygen p manifold. In the case of SrVO$_3$, we will also consider the 14-band $t_{2g} + O_p + e_g$ model.

[1]Department of Physics, University of Fribourg, 1700 Fribourg, Switzerland. [2]Department of Quantum Matter Physics, University of Geneva, Geneva 4, Switzerland. ✉e-mail: ruslan.mushkaev@unifr.ch

This paper is structured as follows: Section II presents the band structures and effective interactions for the tier II calculations, and the results including spectral functions and charge susceptibilities. Section III discusses the most important findings, while Section IV contains a brief outline of the method. A more detailed description of the multi-tier approach and of the susceptibility calculations can be found in the Supplemental Material.

Results

DFT bandstructure and model spaces

The first step in generating the input for the GW+EDMFT self-consistency is to compute the DFT bandstructure of the "full" space, which contains correlation effects through the exchange-correlation potential. This bandstructure allows us to identify a relevant low-energy sector around the Fermi energy to which we can downfold, to be used in the subsequent GW+EDMFT self-consistent calculations.

In the cubic perovskites $SrXO_3$ (where X = V, Cr, Mn), the X cation is enclosed in an Oxygen octahedron, which is in turn enclosed in a Strontium cube. The most relevant low-energy bands around the Fermi level have predominantly t_{2g} character and originate from the X cation's $3d$ orbitals, see the blue bands in Fig. 1. The two higher lying bands are e_g-like and are crystal-field-split from the t_{2g} bands. The 9 lower lying bands originate mainly from the Oxygen p states. At the DFT level, Vanadium, Chromium, and Manganese host 1, 2, and 3 electrons in the t_{2g} bands, respectively. For our tests of the consistency of the method, we will consider the t_{2g}, $t_{2g} + e_g$, and $t_{2g} + O_p$ model spaces (as well as $t_{2g} + O_p + e_g$ for $SrVO_3$), referring to the orbitals contained in the self-consistent (TIER II) subspace, see Fig. 2.

For the TIER I subspace, which is treated with EDMFT, we consider only the subspace of d orbitals, where we expect the strongest correlation effects.

SrVO₃

$SrVO_3$ is a well-studied[9,14–22] metallic perovskite compound, with a near-perfect cubic structure. Experimentally, it is found to be a metal with moderately renormalized conduction bands. Near the Fermi level, photoemission spectroscopy measurements[17] find a reduction of the band velocity by about a factor of two, compared to the LDA bandstructure. The photoemission spectra furthermore reveal an almost dispersionless feature around −1.5 eV, which has been interpreted as a lower Hubbard band[15,16], or as a signal originating primarily from Oxygen vacancies[20]. Inverse photoemission[19] and X-ray absorption spectra[23] reveal a broad peak centered at 2.5–3 eV in the unoccupied part of the spectrum, which could be an upper Hubbard band[15,16], a plasmon sideband[9,21,22], or a feature originating from e_g states[19].

At the LDA level, $SrVO_3$ contains one electron per unit cell in the t_{2g} conduction bands (V $3d_{xy,xz,yz}$ orbitals). Its t_{2g} bands are isolated from the empty e_g bands and the filled Oxygen p bands (see Fig. 1).

In the GW+EDMFT results, shown in Fig. 3, the local t_{2g} DOS displays a prominent quasiparticle peak, moderately renormalized with respect to the LDA DOS, and two side peaks which are not captured by DFT—a weak satellite in the range from −3 to −1 eV and a more prominent broad feature around 2.5–3 eV. To test the consistency of the GW + EMDFT results, we take a closer look at the evolution of the spectral features with increasing size of the self-consistent (SC = Tier II + Tier I) space and check how they compare with experimental data.
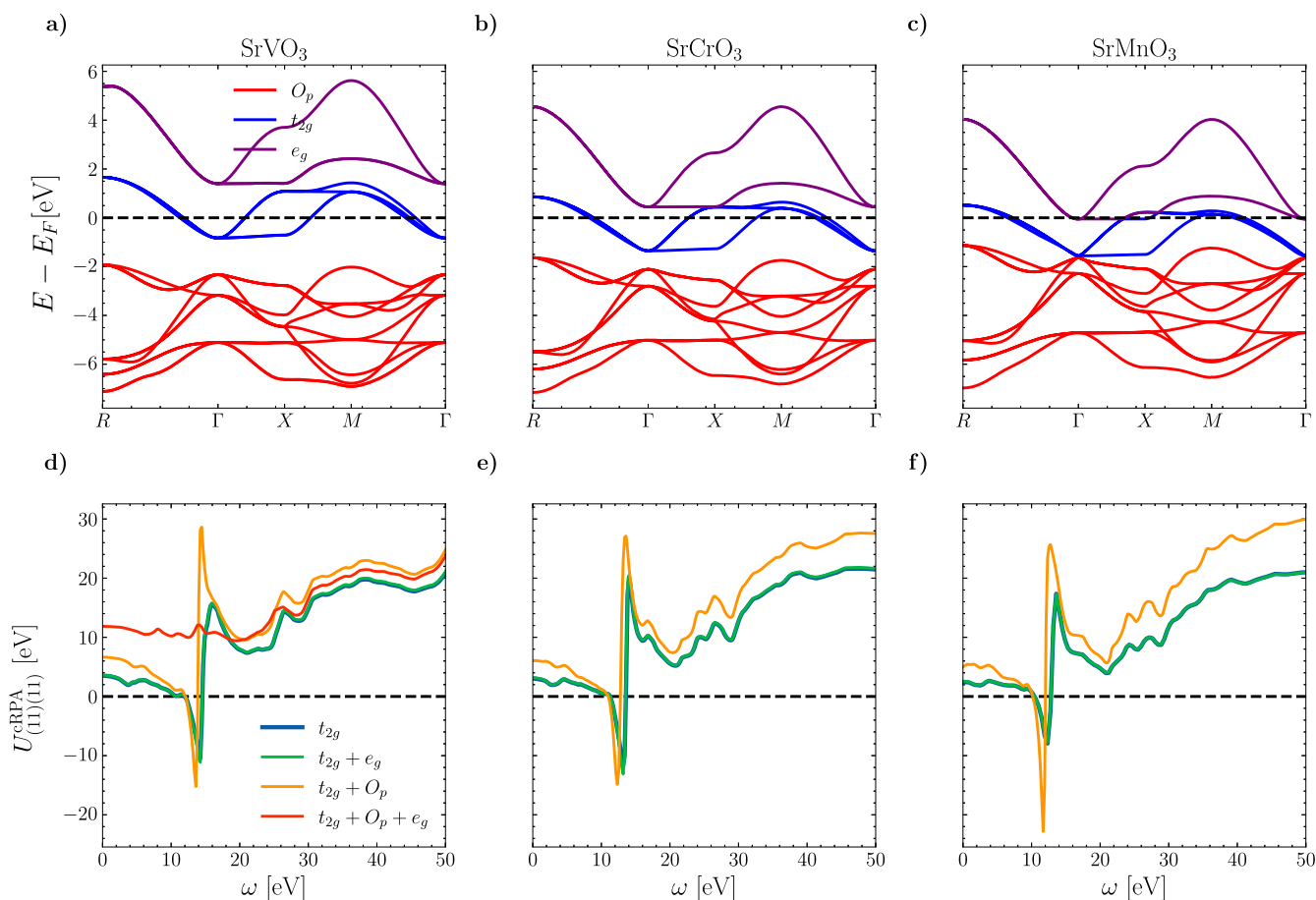
Fig. 1 | DFT bandstructure and cRPA U. a–c DFT-LDA bandstructure of cubic perovskites Sr(V, Cr, Mn)O₃ respectively. The three t_{2g} and two e_g bands originate from the X cation's d-orbitals in the cubic environment. The 9 lower-lying bands originate from Oxygen p-states. **d–f** real part of the intra-orbital cRPA Coulomb interaction U in the t_{2g} manifold for Sr(V, Cr, Mn)O₃ respectively. The high-frequency values of these curves correspond to the bare Coulomb interactions. The pole feature at $\omega \sim 13$ eV in the 3, 5, and 12-band models, which is absent in the 14-band model (see SrVO₃ results) can be attributed to O_p-e_g screening processes.

Fig. 2 | Model spaces. Different model spaces used in the GW+EDMFT simulations of the cubic perovskites. The most correlated t_{2g} and $t_{2g} + e_g$ local subspaces are treated with EDMFT, while their non-local parts, as well as the lower-lying Oxygen p-states are treated by self-consistent GW.
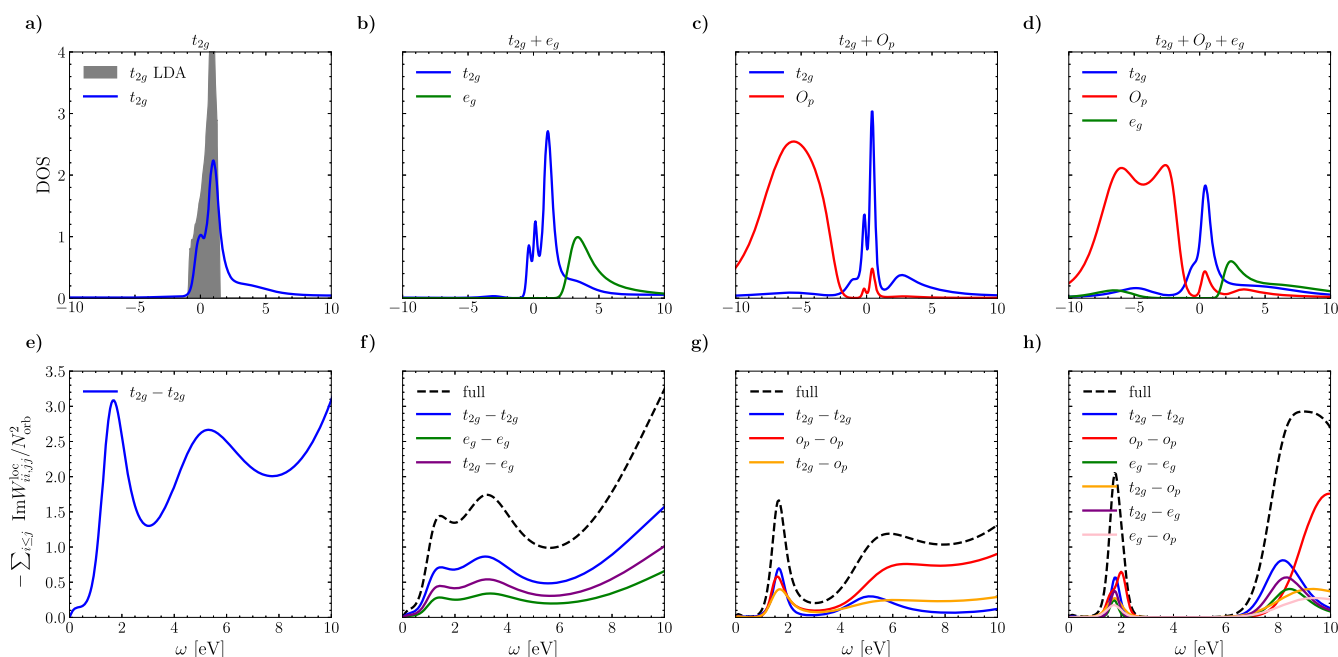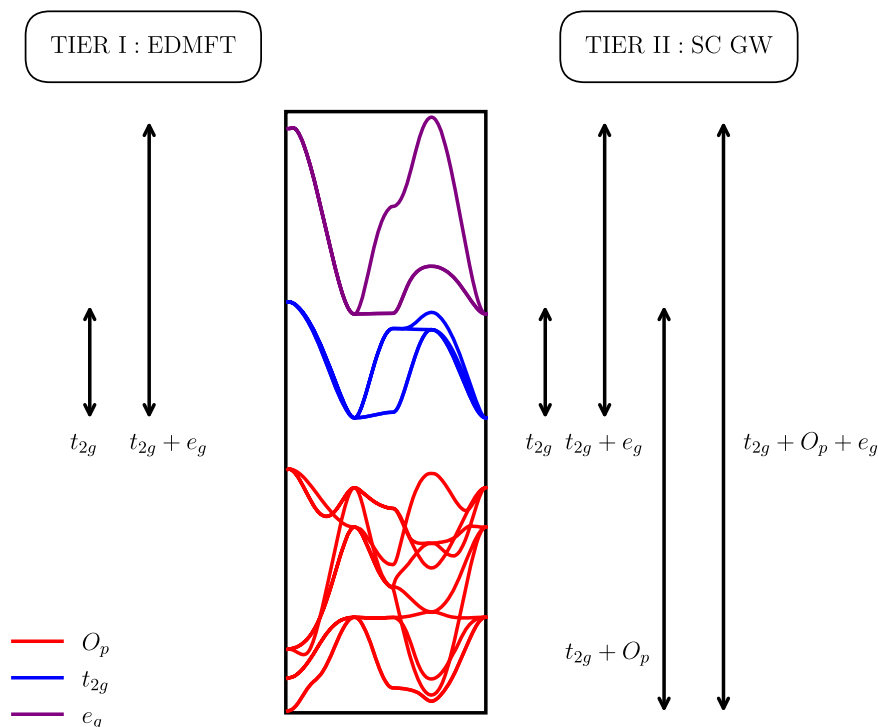
Fig. 3 | Local spectral functions and screened interactions for SrVO₃. a–d Local spectral functions of SrVO₃ computed within 3, 5, 12 and 14-band self-consistent model spaces respectively. All spectra display a central quasiparticle peak along with satellite features in the t_{2g} sector. **e–h** Full and orbital-resolved local screened interactions in 3, 5, 12 and 14-band model spaces computed as a sum of a subset of density-density matrix elements.

The last column of Table 1 reports the GW+EDMFT mass enhancements with respect to the LDA bandstructure, computed as a ratio of Fermi velocities. The corresponding fits to the correlated bands are shown in Fig. 4. We note that while the mass enhancements of 1.0–1.2 are comparable in the t_{2g} and $t_{2g} + e_g$ models, up to the numerical uncertainty of the fitting procedure, the $t_{2g} + O_p$ and $t_{2g} + O_p + e_g$ models yield a stronger mass enhancement of 1.5–1.6, which is closer to the experimental value of $m_{exp}/m_{LDA} \sim 2$[17].

A larger SC space implies an increased degree of localization of the Wannier functions spanning this space and a larger number of screening channels which are excluded in the cRPA construction. As a result, both the bare and screened interactions are larger in the models including O_p, compared to the t_{2g} and $t_{2g} + e_g$ models (see Fig. 1). We list the static ($\omega = 0$) values of the local cRPA and impurity interactions in Table 1. Without the oxygen bands in the model, adding the e_g states to the t_{2g} manifold has little effect on the effective t_{2g} interaction, consistent with previous findings[22].

The impact of the e_g states however increases drastically when we further include the Oxygen states, as evidenced by a significant enhancement of the impurity interaction in the $t_{2g} + O_p + e_g$ model when compared to the $t_{2g} + O_p$ one. This demonstrates the important role of the e_g-O_p screening channels.

For the t_{2g} model, our cRPA static interaction is close to the value of U reported in ref. 21, while the static effective impurity interaction $\mathcal{U}^{static}$ is almost identical to the difference U–V (with V the nearest-neighbor interaction), and hence to the naive estimate of the effective local interaction which takes nonlocal screening into account[24]. This confirms that our GW +EDMFT framework yields meaningful effective interactions.

A second effect, which influences the degree of correlations in our calculations, is the filling of the t_{2g} orbitals (indicated by $N_{t_{2g}}$ in Table 1). Due to the hybridization with Oxygen p states, $N_{t_{2g}}$ in the $t_{2g} + O_p$ and $t_{2g} + e_g + O_p$ models (henceforth referred to as "O_p models") is almost twice the filling of the three band counterpart. The "extra" electron in these models can be found by integrating the t_{2g} local spectral function of Fig. 3 in an energy window covering the Oxygen states.

A comparison between the occupied parts of the local spectral function and photoemission spectroscopy (PES) data from ref. 23 is shown in the top panel of Fig. 5. We note that the occupied part of the quasiparticle peak is well reproduced by all models and that the $t_{2g} + O_p$ spectral function appears to best capture a portion of the incoherent spectral weight (the latter is very broad and weak at ~ −3 eV in the t_{2g} and $t_{2g} + e_g$ models). There is a

widespread view in literature that the feature found in experiments at −1.5 eV represents a lower Hubbard band[15,16]. Its relative amplitude with respect to the quasiparticle peak might however be severely overestimated by the presence of Oxygen vacancies generated by high UV doses[20]. The latter produces states at the same energy as the purported lower Hubbard band.

When compared to experimental PES, the O_p models underestimate the binding energy of the Oxygen states by roughly 1-2 eV, a mismatch that we already find at the level of LDA. Fixing this inaccuracy hence most likely requires a scheme with full charge self-consistency (in TIER III) or some modification of the bandstructure input. The too-strong hybridization with the Oxygen states is also the cause of the strong broadening and inaccurate dispersion of the occupied quasiparticle bands in the O_p models, compared to the experimental data in ref. 20 (top row of Fig. 4). In this comparison, it appears that the position of the renormalized occupied t_{2g} bands (but not their slope at the Fermi level) is better reproduced by the t_{2g} and $t_{2g} + e_g$ models.

The t_{2g} dispersions on a longer momentum path (bottom row of Fig. 4) show similar widths of the occupied t_{2g} bands in all four models, consistent with the local spectra in Fig. 3.
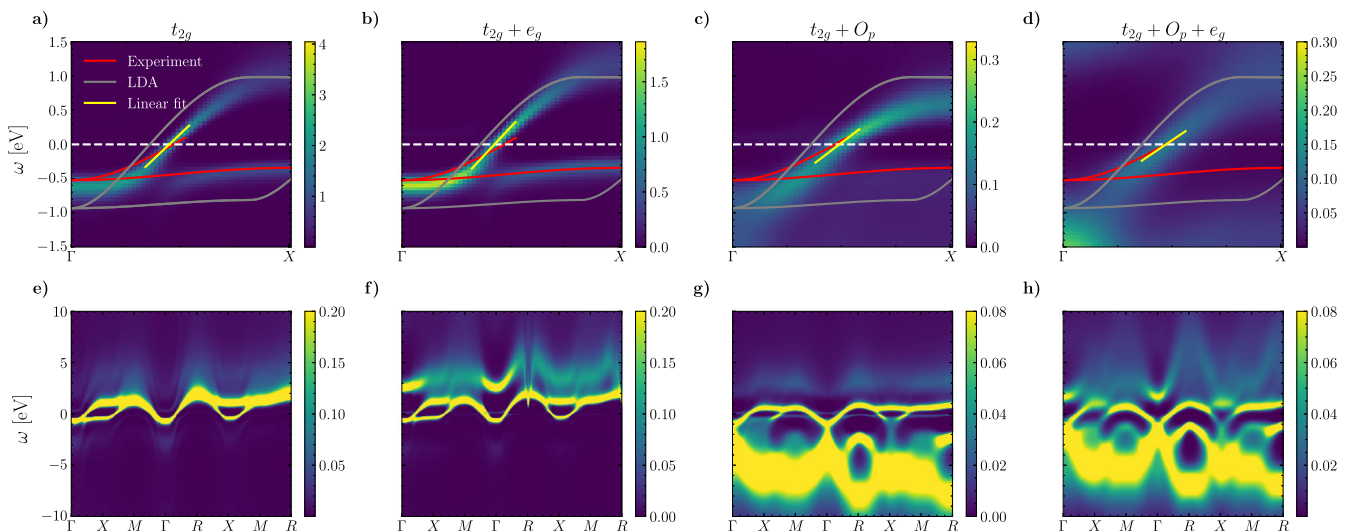
A comparison of the unoccupied parts of the spectral function to Oxygen X-ray absorption spectra (O 1s XAS) from ref. 23 is shown in the bottom panel of Fig. 5. O 1s XAS probes transition from Oxygen core states to orbitals with partial Oxygen character. Since the Oxygens hybridize with the t_{2g} and e_g orbitals, O 1s XAS allows to probe the unoccupied t_{2g} and e_g states. The XAS spectrum has two notable humps at 0.5 and 2.5 eV, respectively, which are in good agreement with the peaks of the O_p models, which explicitly capture the O_p-t_{2g} and O_p-e_g hybridization. The quasiparticle peak in the O_p models is strongly renormalized in the unoccupied part of the spectrum, compared to the t_{2g} and e_g models, which is consistent with the previously noted stronger renormalization of the Fermi velocity. A comparison to the XAS data further shows that this much stronger renormalization is consistent with experiment.

Plasmon satellites and loss function of SrVO₃

The nature of the spectral feature at around 3 eV is still under debate[19,22]. It has been interpreted as an upper Hubbard band[16], or as a (sub)plasmon feature originating from charge excitations within the $3d$ manifold[10]. GW +EDMFT, which treats correlation and screening effects in a self-consistent manner, should be a useful tool for distinguishing between these two
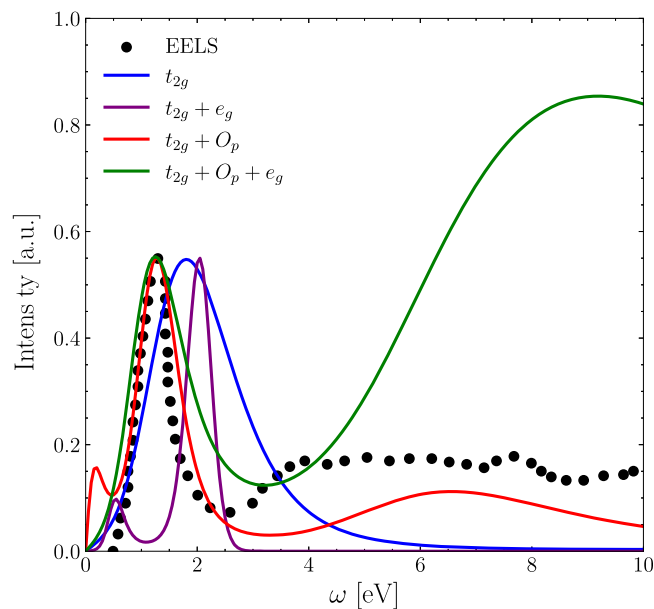
Table 1 | Fillings, quasiparticle weights, atomic gaps, interaction parameters, and mass enhancements for SrVO₃

	t_{2g}	$t_{2g} + e_g$	$t_{2g} + O_p$	$t_{2g} + O_p + e_g$
$N_{t_{2g}}$	1.00	0.87	1.91	1.95
$Z^{EDMFT}_{t_{2g}}$	0.61	0.64	0.36	0.43
Δ_{at} [eV]	1.5	1.6	3.6	8.1
$\mathcal{U}^{static}_{t_{2g}}$ [eV]	2.7	2.8	5.1	9.6
$\mathcal{J}^{static}_{t_{2g}}$ [eV]	0.4	0.4	0.5	0.5
$U^{cRPA}_{t_{2g}}$ [eV]	3.5	3.6	6.6	11.8
$\frac{m_{GW+EDMFT}}{m_{LDA}}$	1.2	1.0	1.5	1.6

Fig. 4 | Momentum-resolved spectral functions for SrVO₃. a–d Momentum resolved correlated bandstructure along the indicated path, and comparison to the peak intensity of the momentum resolved photoemission spectrum reported in ref. 20 (red lines) in 3, 5, 12 and 14-band model spaces. The mass renormalizations (with respect to the LDA values) in Table 1 are extracted from linear fits of the Fermi velocity (yellow lines). **e–h** Momentum resolved spectral function on the full path in the Brillouin zone in 3, 5, 12 and 14-band model spaces.

a)

b)
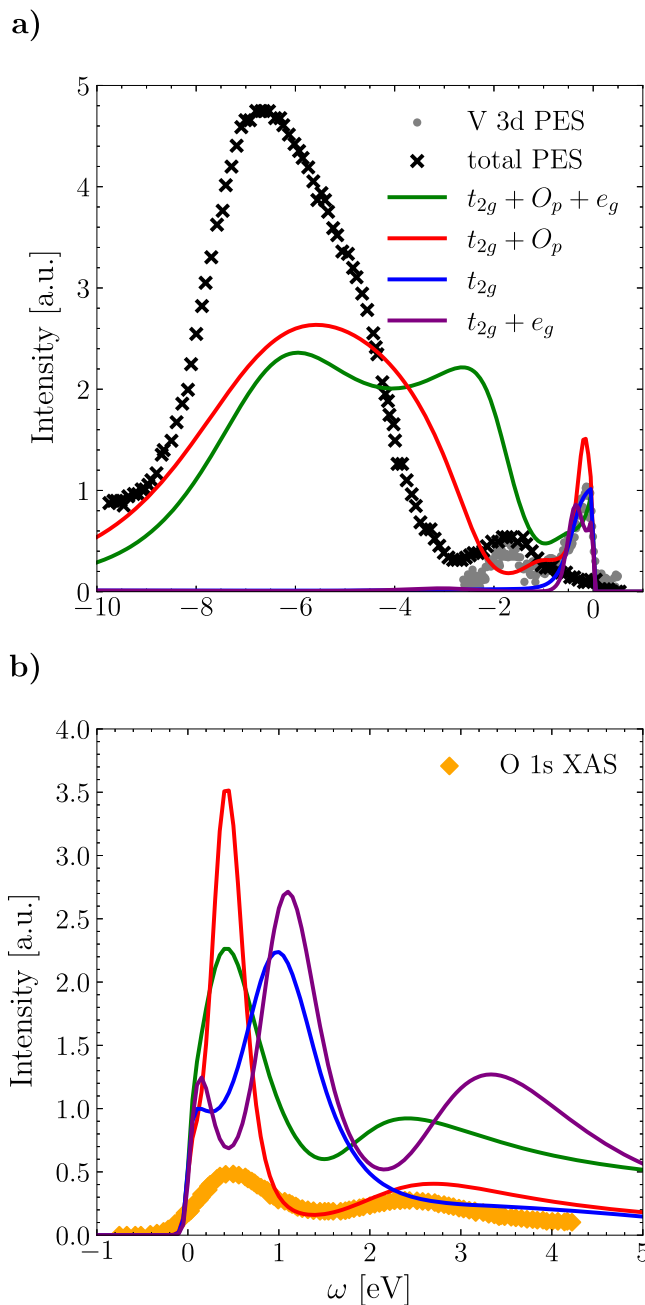
Fig. 5 | Comparison to XAS/PES for SrVO₃. Comparison of local spectral functions to experimental PES (**a**) and XAS spectra (**b**) from ref. 23 for SrVO₃. The total and V 3d PES have been measured at $T = 80$ K and $T = 20$ K respectively. The calculated spectral functions have been multiplied by the Fermi–Dirac function $f(\omega)$ for $T = 20$ K and by $1 - f(\omega)$ for $T = 298$ K in the occupied and unoccupied regions, respectively.

Fig. 6 | Local loss function for SrVO₃. Local loss function $-\mathrm{Im}\sum_q \frac{1}{\epsilon(q,\omega)}$ in different model spaces. Black dots show the experimental values[42] integrated over the momentum range $0 < q < 4\,\text{Å}^{-1}$. The calculated curves have been rescaled to match the experimental peak height.

case to rule out a Hubbard band interpretation. These findings are consistent with the analysis of the t_{2g} and $t_{2g} + e_g$ models in refs. 9,22.
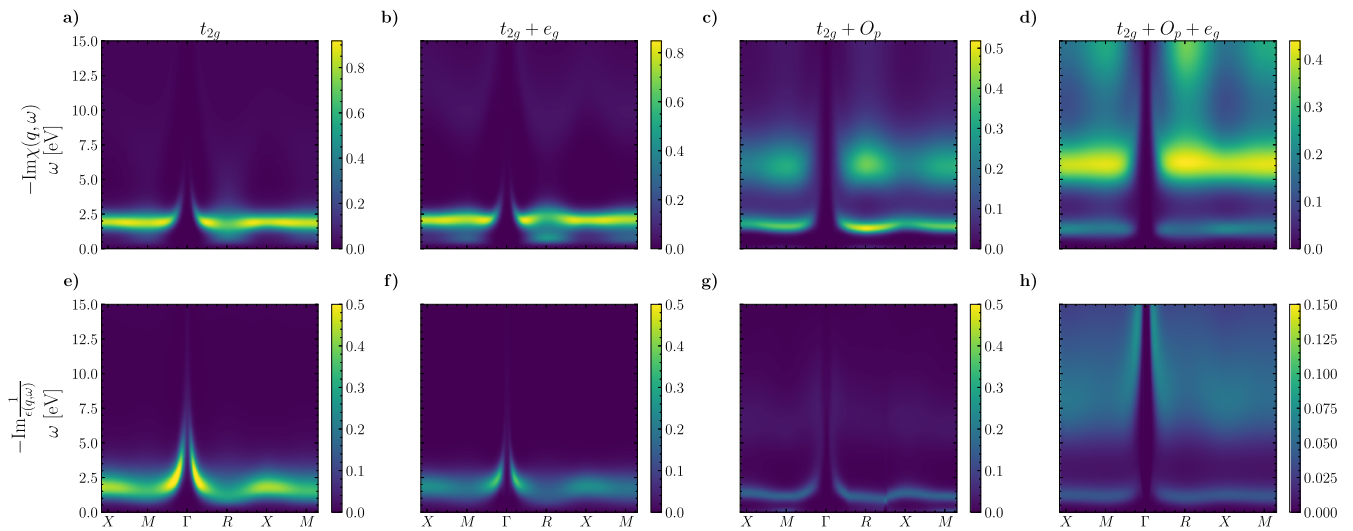
To test the plasmon scenario as a possible explanation for the high energy spectral feature, we focus on the imaginary part of the local screened interaction W^{loc}, reported in the bottom row of Fig. 3, and the loss function $-\mathrm{Im}\sum_q \frac{1}{\epsilon(q,\omega)}$ shown in Fig. 6. W^{loc} features two low energy peaks between 0 and 10 eV in all model spaces. For the t_{2g} and $t_{2g} + e_g$ models, the calculated loss function does not feature the peak above 3 eV, present in the screened interaction, suggesting that the peak in W^{loc} for these models should originate directly from U_{cRPA}, which implicitly (through the downfolding) contains the Oxygen screening and whose spectrum indeed has a feature in this energy range, as evidenced in the plot of $U_{\text{cRPA}}^{(11),(11)}$ in Fig. 1.

When the Oxygen states are explicitly included, the loss function recovers the higher energy peak, in reasonable agreement with that of W^{loc} for the O_p models, implying that the upper lying peak is mostly due to Oxygen states. This is also evidenced by its dominant Oxygen character (Fig. 3). The large upper peak in the $t_{2g} + O_p + e_g$ loss function can be traced back to the large O_p-e_g pole in U^{cRPA} in the 3-, 5- and 12-band models (bottom left of Fig. 1), which is now explicitly included in the screening channels of the 14-band model, captured by the loss function. Its relative amplitude is severely overestimated when compared to experiment, potentially due to an improper account of selection rules.

The lower lying experimental peak at ~1.5 eV is captured rather well by all models and is mostly of V d character, with some contribution from the O p states.

A plasmonic excitation should manifest itself as a faint replica of the quasiparticle bandstructure, separated by the plasmon frequency (pole of the local screened interaction). A plasmon feature in the local fermionic spectral function would then be expected at $\omega_{\text{qp}} + \omega_{\text{pl}}$, where ω_{qp} is the position of the quasiparticle peak and ω_{pl} the energy of one of the poles in $\mathrm{Im}\,W^{\text{loc}}$. Such satellite features are indeed evident in the momentum resolved spectra shown in Fig. 4, which resemble the GW + cumulant expansion results in ref. 21.

More quantitatively, taking the lowest energy poles of W^{loc} at 1.7, 1.4, 1.7, and 1.4 eV for the t_{2g}, $t_{2g} + e_g$, $t_{2g} + O_p$ and $t_{2g} + O_p + e_g$ models, respectively, $\omega_{\text{qp}} + \omega_{\text{pl}}$ is roughly at ~2.7, 2.5, 2.1 and 2.8 eV. These values

scenarios. Assuming that the satellite in the occupied part of the spectrum is the lower Hubbard band, the tentative upper Hubbard band position can be estimated from the static limit of the effective local interaction. The Mott gap in the atomic limit is $\Delta_{\text{at}} := E_{N+1} - 2E_N + E_{N-1}$, where N is the electron population of the t_{2g} manifold and the lowest energies E_N in the different charge sectors are obtained via Exact Diagonalization (ED) of a Kanamori-type Hamiltonian for the t_{2g} orbitals. Comparing the atomic gap values in Table 1 to the separation between the lower and upper satellites in the local DOS (Fig. 3) shows that the separations are too large/small with respect to the atomic gap values in all models, with the exception of the $t_{2g} + O_p$ model. There Δ_{at} is compatible with the subband splitting, making it difficult in this

Fig. 7 | Momentum-resolved charge susceptibility and loss function for SrVO₃. Momentum resolved charge susceptibility: (**a–d**) and loss function: (**e–h**) for SrVO₃ in the 3, 5, 12 and 14-band model spaces respectively. The region in the vicinity of the R point for the dielectric function in the $t_{2g} + O_p$ model has been interpolated due to numerical noise. The effective bare interaction used in the susceptibility calculation for the $t_{2g} + O_p + e_g$ model has been renormalized by a factor of two to improve the convergence of the RPA series.

are compatible with the energy region of the right-most hump in the fermionic DOS (top row of Fig. 3).

There is thus substantial evidence for interpreting the satellite in the unoccupied spectrum as a (sub-)plasmonic excitation. The dispersion of the plasmon is depicted in Fig. 7, which plots the charge susceptibility alongside the momentum-resolved loss function, which should diverge for plasmonic excitations. The negative curvature around the Γ point can be likely attributed to band-structure effects similar to those occurring in transition metal dichalcogenides[25,26].

The orbital make-up of the low-energy plasmonic excitation is mostly composed of t_{2g}-t_{2g} and t_{2g}-e_g excitations in all models (see the orbital-resolved plots of W_{loc} in Fig. 3), although excitations involving O_p states also remain competitive, likely due to t_{2g}-O_p and e_g-O_p hybridization.

SrCrO₃
SrCrO₃ is a less-studied compound, whose ground state is still under debate due to a difficult high-pressure synthesis procedure. The first experimental measurements[27] suggested that SrCrO₃ is a paramagnetic metal, while more recent results[28] reported a paramagnetic insulating behavior. EELS measurements performed in ref. 29 indicate a paramagnetic metal. These experimental results contradict the numerical DFT calculations in ref. 30, which predicted a rare antiferromagnetic (AFM) weakly correlated metallic phase, which was later supported by X-ray and O 1s XAS data[31]. A recent DFT + DMFT investigation[32] found that SrCrO₃ can potentially host a charge disproportionated meta-stable insulating state, although implementing charge self-consistency yielded a

metallic solution. It is thus interesting to apply the *GW*+EDMFT machinery to this compound.

At the LDA level, there are 2 electrons in the t_{2g} derived bands. *GW* +EDMFT yields similar occupations for the t_{2g} and $t_{2g} + e_g$ models, while the t_{2g}-like orbitals are almost half-filled in the $t_{2g} + O_p$ model, see Table 2. The static $\mathcal{U}_{t_{2g}}$ values are smaller than in the case of SrVO₃, but since the filling is larger, the correlation effects are stronger, as indicated by the smaller quasiparticle weight.
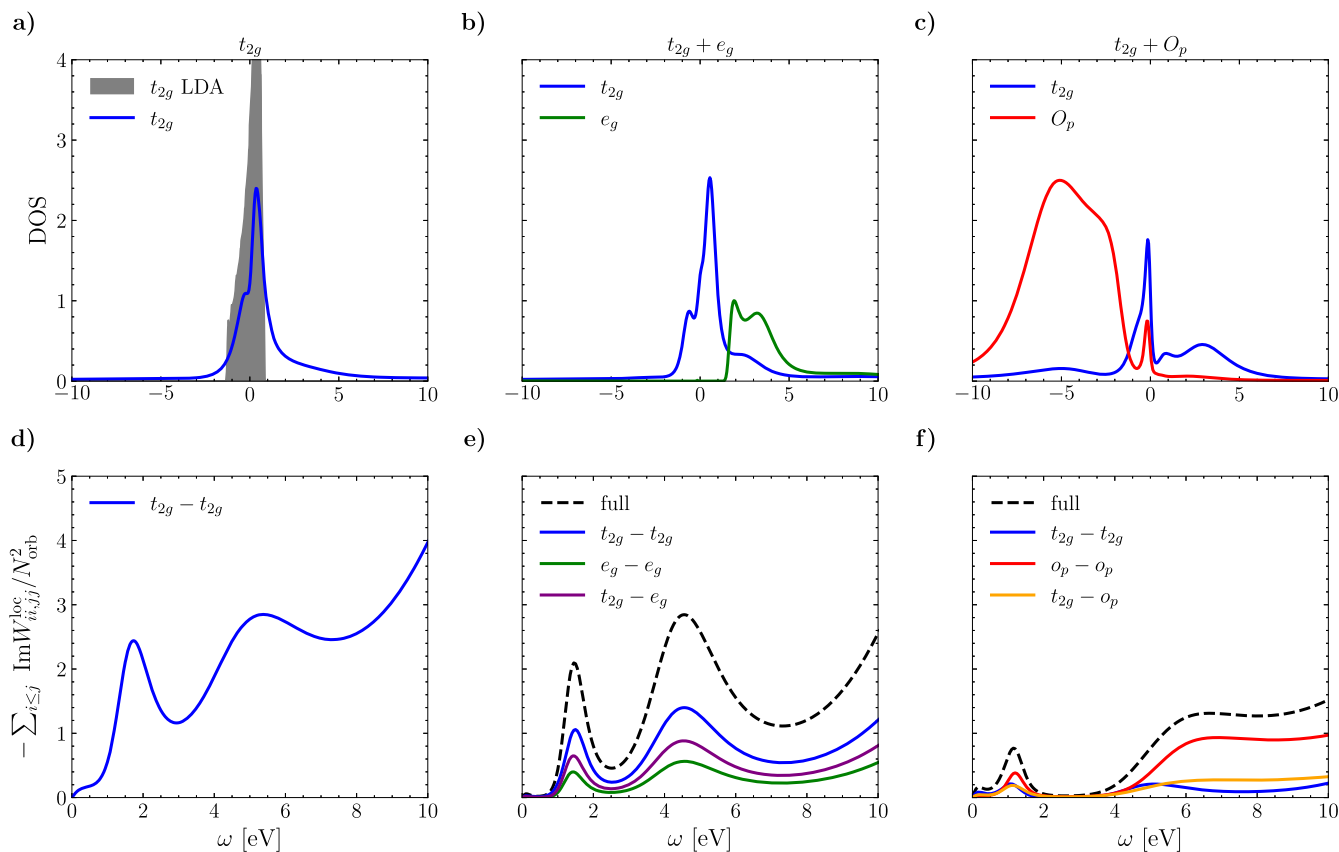
The local fermionic spectral functions are plotted for the three models in the top row of Fig. 8. All the solutions are metallic (we restrict our calculation here to the paramagnetic phase). Again, due to stronger bare interactions and larger filling, the renormalization of the t_{2g} bands is more pronounced in the $t_{2g} + O_p$ model than in the other two models.

The local t_{2g} spectra show satellites below and above the quasiparticle peak, but in the case of the 3- and 5-band models, a comparison between the energy splitting and the atomic gap Δ_{at} (Table 2) shows that these cannot be interpreted as Hubbard bands. The corresponding local screened interaction is plotted in the bottom row of Fig. 8. The lowest energy pole in ImW^{loc} at energy $\omega_{pl} = 1.5$–1.7 eV is compatible with the satellite feature in the fermionic spectra around ~2 eV, and appears to contribute also to the very weak satellite on the occupied side of the spectrum, consistent with the plasmon interpretation. The second lowest pole at energy $\omega_{pl} \approx 5$ eV may furthermore contribute to the broad tails of the satellites, although in the $t_{2g} + O_p$ case, these contributions are masked by the hybridization with the Oxygen bands (occupied part), and by a possible upper Hubbard band feature (unoccupied part).

Figure 9 shows a comparison of the occupied and unoccupied spectral functions to the experimental spectra from ref. 31 in the top and bottom panels, respectively. The occupied part of the spectrum has been probed with X-ray photoemission spectroscopy (XPS/HAXPES)[31] and the unoccupied part with O 1s XAS. We note a very good agreement for the $t_{2g} + O_p$ model, which is able to reproduce all features in the occupied Oxygen and in the unoccupied $t_{2g} + O_p$ spectrum. Only the presence of a quasiparticle peak is not confirmed by the experiments, but as mentioned above, the experimental situation concerning the metallic or insulating behavior is not yet settled. Nevertheless, we note that for all models, the width of the occupied quasiparticle peak is comparable to the extent of the right-most step feature between -1 and 0 eV in the experimental spectra, which supports the theoretically predicted metallic solution. The first peak near 0.8 eV in the O 1s XAS spectra could be associated either with the first satellite in the

Table 2 | Fillings, quasiparticle weights, atomic gaps, interaction parameters, and mass enhancements for SrCrO₃

	t_{2g}	$t_{2g} + e_g$	$t_{2g} + O_p$
$N_{t_{2g}}$	2.00	1.83	2.95
$Z_{t_{2g}}$ (from Σ^{EDMFT})	0.50	0.54	0.16
Δ_{at} [eV]	1.4	1.1	5.8
$\mathcal{U}_{t_{2g}}^{static}$ [eV]	2.3	2.3	4.6
$\mathcal{J}_{t_{2g}}^{static}$ [eV]	0.3	0.4	0.6
$U_{t_{2g}}^{cRPA}$ [eV]	3.0	3.2	6.1

Fig. 8 | Local spectral functions and screened interactions for SrCrO₃. a–c local fermionic spectral functions of SrCrO₃ computed within 3, 5 and 12-band self-consistent model spaces, respectively. **d–f** bosonic spectra (screened interaction) within 3, 5 and 12-band model spaces. In the case of the $t_{2g} + e_g$ and $t_{2g} + O_p$ models, the contributions from different subsets of density-density matrix elements to $\mathrm{Im}\,W^{\mathrm{loc}}$ are shown by solid lines.

$t_{2g} + O_p$ model spectrum, or with the much broader quasiparticle peak in the t_{2g} and $t_{2g} + e_g$ spectra. Similarly, the second broader satellite near 3 eV, which perfectly agrees in position and shape with the $t_{2g} + O_p$ spectrum, could originate also from e_g states, as seen from the comparison to the corresponding hump in the $t_{2g} + e_g$ spectrum. A signal from the e_g states is expected in the O 1s XAS spectra, since the Oxygen states also hybridize with the e_g orbitals.

SrMnO₃

SrMnO₃ is an insulating, antiferromagnetic perovskite compound, with a Néel temperature $T_{\mathrm{Néel}}$ between 233 K[33] and 266 K[34].

Its Manganese cation hosts 3 d-electrons in the unit cell, which at the LDA level occupy almost entirely the t_{2g} bands (Fig. 1). In paramagnetic GW+EDMFT calculations at $T > T_{\mathrm{Néel}}$, the local spectral function exhibits metallic behavior, with a quasiparticle peak in the vicinity of the Fermi level (Fig. 10), for all the low-energy subspaces considered. Upon removing the TIER III ($G^0 W^0$) self-energy contribution (which contains metallic screening from the DFT bandstructure), however, one recovers an electronic gap (bottom row of Fig. 10). This suggests a sensitivity of the method to the DFT starting point since the metallicity of the DFT solution affects the GW+EDMFT result even after self-consistency.

While the gap is missing in the full calculation, we may nevertheless proceed with the analysis of the higher-energy structures in the local spectral function. Here, we note the appearance of satellites in the $t_{2g} + e_g$ and $t_{2g} + O_p$ model spectra, whose separation is in good agreement with the gap Δ_{at} computed in the atomic limit via ED, see Table 3 and the arrows in Fig. 10. We thus interpret these features as Hubbard bands. The Hubbard satellites cannot be resolved in the t_{2g} model, but they become prominent once we add the e_g states. This shows that the e_g states have a significant effect on the low-energy screening in SrMnO₃, and hence on the correlation

strength, as confirmed by the static impurity interaction values in Table 3. A more active role of the e_g states, compared to SrVO₃ and SrCrO₃, is already expected from the LDA bandstructure (Fig. 1), where the e_g bands for SrMnO₃ overlap with the t_{2g} bands.
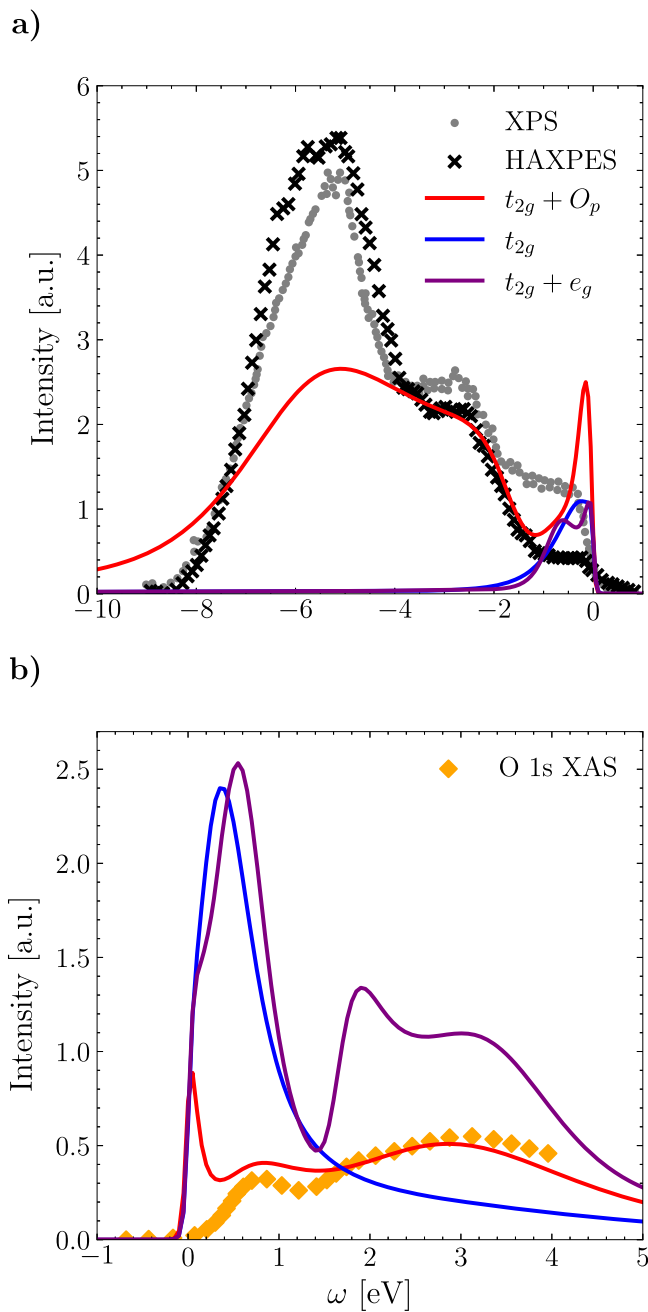
Incorporating the Oxygen orbitals into the SC space again results in a jump in the filling of the t_{2g} orbitals, as in the case of SrVO₃: the t_{2g} shell now has nominally one extra electron coming from the hybridization with the Oxygens (see the prominent hump in Fig. 10 at $\omega \approx -5$ eV). The quasiparticle weight, estimated from Σ^{EDMFT} undergoes a substantial renormalization by a factor of two, compared to the t_{2g} model, which is more pronounced than what we observed for SrVO₃.

Discussion

We have systematically tested the multi-tier GW+EDMFT framework on the perovskite compounds SrXO₃ (X=V, Cr, Mn) by comparing the low-energy electronic structures calculated in different energy windows. If the downfolding to these model subspaces, as well as the solutions of the corresponding many-body problems, were implemented with exact methods, the results would be consistent by construction (up to hybridization effects).

For practical reasons, the downfolding has been implemented here via cRPA and single-shot $G_0 W_0$, while TIER II is treated at the GW level (with local vertex corrections), and TIER I at the EDMFT level (with density-density interactions). It is thus interesting to test to what extent this ab-initio framework produces consistent results for different model spaces. While inaccuracies may be expected for very small low-energy subspaces, one would expect systematic improvements as the self-consistently solved model spaces are enlarged.

To judge if this is indeed the case, we compared the calculated results to available PES and XAS data. For SrVO₃, GW+EDMFT predicts a moderately correlated metallic phase in all model spaces, with the O_p models

a)

b)

Fig. 9 | Comparison to XAS/PES for SrCrO₃. Comparison of the local spectral functions to the experimental XPS/HAXPES (**a**) and XAS (**b**) spectra extracted from ref. 31. The spectral functions have been multiplied by the Fermi–Dirac function $f(\omega)$ and by $1 - f(\omega)$ (assuming the temperature $T = 298$ K) in the upper and lower panels, respectively.

Table 3 | Fillings, quasiparticle weights, atomic gaps, interaction parameters, and mass enhancements for SrMnO₃

	t_{2g}	$t_{2g} + e_g$	$t_{2g} + O_p$
$N_{t_{2g}}$	3.00 (3.00)	2.79 (3.00)	3.97 (3.16)
$Z_{t_{2g}}$	0.36	0.43	0.18
Δ_{at} [eV]	2.7 (3.1)	3.6 (3.3)	2.3 (6.2)
$\mathcal{U}^{static}_{t_{2g}}$ [eV]	2.1 (2.3)	2.5 (2.5)	4.1 (4.8)
$\mathcal{J}^{static}_{t_{2g}}$ [eV]	0.3 (0.4)	0.3 (0.4)	0.6 (0.7)
$U^{cRPA}_{t_{2g}}$ [eV]	2.3	2.6	5.0

The values in brackets are for a calculation without the TIER III self-energy contribution, which yields an insulating solution.

$t_{2g} + O_p$ calculations is about 1 eV too high, compared to the PES data, but this is already the case in the LDA input. Our calculations are not self-consistent in TIER III, and a charge self-consistent implementation could potentially correct this inaccuracy.

In the case of SrCrO₃, we have demonstrated an excellent agreement between the $t_{2g} + O_p$ model results and the available XPS and O 1s XAS data for the Oxygen and unoccupied t_{2g} states, while the signature of the quasiparticle peak is not clearly seen in XPS. The low-energy peak in the O 1s XAS would however be equally consistent with the (much wider) quasiparticle band of the t_{2g} and $t_{2g} + e_g$ models so that it is not clear in this case if the stronger correlation effects in the $t_{2g} + O_p$ description improve the agreement with experiment. Again, the high-energy satellite near 3 eV overlaps with the e_g states, so that the XAS signal presumably detects not only the plasmon satellite of the t_{2g} bands but also the e_g states.
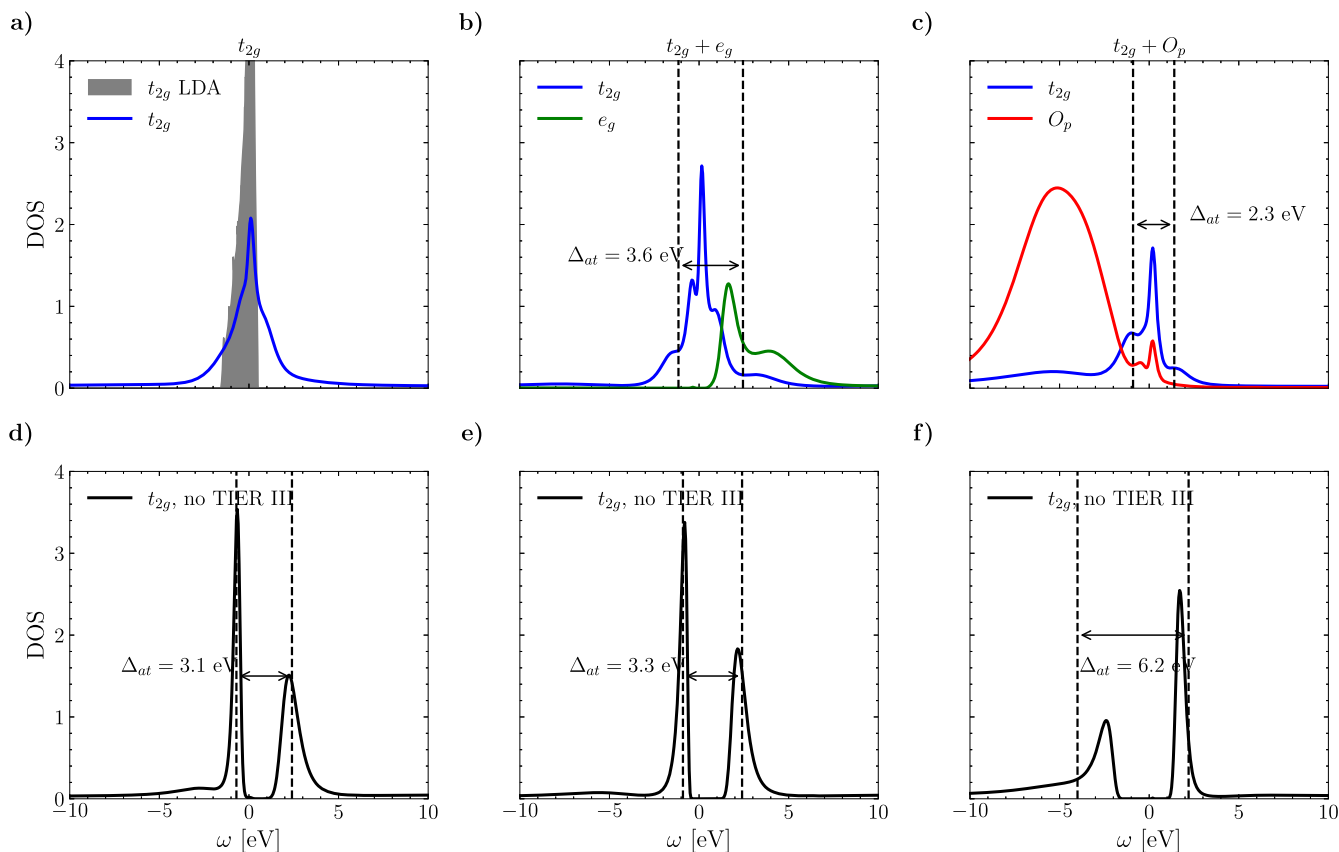
For SrMnO₃, our paramagnetic calculations in all three model subspaces predict a metallic system, likely caused by the metallicity of the DFT starting point.

Our $t_{2g} + e_g$ and $t_{2g} + O_p$ simulations produced Hubbard bands in the (metallic) spectra, in contrast to the t_{2g}-only calculations. This shows that in this system, the e_g states (which are very close to the Fermi level) play a relevant role in the low-energy screening of the t_{2g} electrons[22].

Overall, our calculations demonstrated a fair agreement between the first-principles results for the different model subspaces, and between the calculated and experimentally measured data, bearing in mind the absence of adjustable parameters in GW+EDMFT. Our study, however, also showed that there exist significant discrepancies between the results from the $t_{2g}(+e_g)$ and O_p model spaces, with the latter exhibiting stronger correlation effects. In general, the Oxygen atoms in d-electron perovskites are responsible for the octahedral crystal field splitting of the d-orbitals. The O 2p states hybridize with the d-states, with stronger hybridization for the early transition metals, where the e_g orbitals remain empty (a filling of the e_g orbitals increases the lattice parameter w.r.t. the orbital radii, which reduces the hybridization[35]). Explicitly including Oxygens at the GW level in O(GW) + t_{2g}(GW+EDMFT) calculations results in a significant enhancement of the t_{2g} occupations (one needs to keep in mind that these t_{2g} orbitals also extend to the Oxygen sites), compared to the d-models, leading to stronger correlation effects, as evidenced by smaller quasiparticle weights $Z_{t_{2g}}$ and larger values of $\mathcal{U}^{static}_{t_{2g}}$. Including further local Oxygen correlations at the EDMFT level in O(GW+EDMFT) + t_{2g}(GW+EDMFT) calculations, which amounts to solving 1(V) + 3(O) = 4 impurity problems for SrVO₃, yielded no substantive change (see Supplementary Fig. 1). In particular, the position of the O states, as well as the width of the quasiparticle and O bands do not change significantly. This indicates that it is sufficient to treat the Oxygen states at the GW level (as one might expect for almost filled p bands).

The observation that the $t_{2g} + O_p$ and $t_{2g} + e_g + O_p$ calculations are in overall better agreement with the experiments hints at an overestimation of screening in the cRPA downfolding. An accurate treatment

yielding mass enhancements closest to experiment. The reduced band velocity near the Fermi level is a consequence of a strong renormalization of the bands in the unoccupied part of the spectrum, while in the occupied part, the t_{2g} and $t_{2g} + e_g$ models actually produce a better agreement with the PES measurements along the Γ-X path. The much stronger renormalization of the unoccupied bands in the O_p models is consistent with the O 1s XAS spectrum, which due to hybridization between the O_p and t_{2g}/e_g orbitals provides information on the unoccupied d states. The much discussed satellite at -1.5 eV in the local spectra (which has been interpreted as a lower Hubbard band or as a signal from Oxygen vacancies) is weakly present as a shoulder feature at -1 eV in the O_p models, while the satellite around 3 eV could be interpreted as a plasmon. The position of the Oxygen bands in the

Fig. 10 | Local spectral functions for SrMnO₃. Local fermionic spectral functions of $SrMnO_3$ in the paramagnetic state, computed within the 3, 5 and 12-band model spaces with (**a–c** respectively) and without (**d–f**) the TIER III self-energy contribution. The atomic gap values from Table 3 are indicated by the arrows.

of screening from low-energy bands may require more sophisticated downfolding schemes[13,36].

Methods

Input generation

The DFT calculations were performed with the all-electron full-potential linearized augmented plane-wave (FLAPW) code FLEUR[37] on a $20 \times 20 \times 20$ **k**-point mesh, and the cRPA and G^0W^0 downfolding with a customized SPEX code[38]. Wannier functions from the Wannier90 library[39] were used to define the models.

GW+EDMFT

The self-consistent multi-tier GW+EDMFT calculations were performed with the implementation described in refs. 9,10, using a CT-HYB quantum impurity solver for multi-orbital models with retarded density-density interactions[40,41]. To further capture spin fluctuations in a self-consistent manner requires impurity solvers which can additionally handle retarded spin-spin interactions, which are currently unavailable. A detailed description of the method can be found in the Supplementary Material. A $10 \times 10 \times 10$ **k**-point grid and an inverse temperature of $\beta = 10$ eV^{-1} with 477 Matsubara frequencies were used in all self-consistent GW-EDMFT calculations, apart from the 14-band model which was done at $\beta = 5$ eV^{-1} with 238 Matsubara frequencies due to computational constraints. The charge susceptibilities and dielectric functions were computed with the procedures described in the Supplementary Material, which also contains additional plots such as the RPA spin susceptibility (Supplementary Fig. 2) and a comparison of the self-energies (Supplementary Fig. 3).

Data availability

Code availability

References

1. Dagotto, E. Complexity in strongly correlated electronic systems. *Science* **309**, 257–262 (2005).
2. Hohenberg, P. & Kohn, W. Inhomogeneous electron gas. *Phys. Rev.* **136**, B864–B871 (1964).
3. Kohn, W. & Sham, L. J. Self-consistent equations including exchange and correlation effects. *Phys. Rev.* **140**, A1133–A1138 (1965).
4. Georges, A., Kotliar, G., Krauth, W. & Rozenberg, M. J. Dynamical mean-field theory of strongly correlated fermion systems and the limit of infinite dimensions. *Rev. Mod. Phys.* **68**, 13–125 (1996).
5. Haule, K. & Birol, T. Free energy from stationary implementation of the DFT + DMFT functional. *Phys. Rev. Lett.* **115**, 256402 (2015).
6. Shim, J. H., Haule, K. & Kotliar, G. Modeling the localized-to-itinerant electronic transition in the heavy fermion system CeIrIn₅. *Science* **318**, 1615–1617 (2007).
7. Karolak, M. et al. Double counting in LDA+DMFT—the example of NiO. *J. Electron Spectrosc. Relat. Phenom.* **181**, 11–15 (2010).
8. Biermann, S., Aryasetiawan, F. & Georges, A. First-principles approach to the electronic structure of strongly correlated systems: combining the GW approximation and dynamical mean-field theory. *Phys. Rev. Lett.* **90**, 086402 (2003).

9. Boehnke, L., Nilsson, F., Aryasetiawan, F. & Werner, P. When strong correlations become weak: consistent merging of GW and DMFT. *Phys. Rev. B* **94**, 201106 (2016).

10. Nilsson, F., Boehnke, L., Werner, P. & Aryasetiawan, F. Multitier self-consistent $GW + EDMFT$. *Phys. Rev. Mater.* B, 043803 (2017).

11. Kang, B., Semon, P., Melnick, C., Kotliar, G. & Choi, S. Comdmft v.2.0: Fully self-consistent ab initio gw+edmft for the electronic structure of correlated quantum materials. *arXiv:2310.04613* (2023).

12. Hedin, L. New method for calculating the one-particle green's function with application to the electron-gas problem. *Phys. Rev.* **139**, A796–A823 (1965).

13. Honerkamp, C., Shinaoka, H., Assaad, F. F. & Werner, P. Limitations of constrained random phase approximation downfolding. *Phys. Rev. B* **98**, 235151 (2018).

14. Morikawa, K. et al. Spectral weight transfer and mass renormalization in mott-hubbard systems $SrVO_3$ and $CaVO_3$: influence of long-range Coulomb interaction. *Phys. Rev. B* **52**, 13711–13714 (1995).

15. Sekiyama, A. et al. Mutual experimental and theoretical validation of bulk photoemission spectra of $Sr_{1-x}Ca_xVO_3$. *Phys. Rev. Lett.* **93**, 156402 (2004).

16. Pavarini, E. et al. Mott transition and suppression of orbital fluctuations in orthorhombic $3d^1$ perovskites. *Phys. Rev. Lett.* **92**, 176403 (2004).

17. Yoshida, T. et al. Direct observation of the mass renormalization in $SrVO_3$ by angle resolved photoemission spectroscopy. *Phys. Rev. Lett.* **95**, 146404 (2005).

18. Sakuma, R., Werner, P. & Aryasetiawan, F. Electronic structure of $SrVO_3$ within GW+DMFT. *Phys. Rev. B* **88**, 235110 (2013).

19. Tomczak, J. M., Casula, M., Miyake, T. & Biermann, S. Asymmetry in band widening and quasiparticle lifetimes in $SrVO_3$: competition between screened exchange and local correlations from combined GW and dynamical mean-field theory $GW + DMFT$. *Phys. Rev. B* **90**, 165138 (2014).

20. Backes, S. et al. Hubbard band versus oxygen vacancy states in the correlated electron metal $SrVO_3$. *Phys. Rev. B* **94**, 241110 (2016).

21. Nakamura, K., Nohara, Y., Yosimoto, Y. & Nomura, Y. Ab initio gw plus cumulant calculation for isolated band systems: application to organic conductor $(TMTSF)_2pf_6$ and transition-metal oxide $SrVO_3$. *Phys. Rev. B* **93**, 085124 (2016).

22. Petocchi, F., Nilsson, F., Aryasetiawan, F. & Werner, P. Screening from e_g states and antiferromagnetic correlations in $d^{(1, 2, 3)}$ perovskites: a $GW + EDMFT$ investigation. *Phys. Rev. Res.* **2**, 013191 (2020).

23. Inoue, I. et al. Systematic change of spectral function observed by controlling electron correlation in $Ca_{1-x}Sr_xVO_3$ with fixed 3d1 configuration. *Phys. C. Supercond.* **235-240**, 1007–1008 (1994).

24. Schüler, M., Rösner, M., Wehling, T. O., Lichtenstein, A. I. & Katsnelson, M. I. Optimal Hubbard models for materials with nonlocal coulomb interactions: graphene, silicene, and benzene. *Phys. Rev. Lett.* **111**, 036601 (2013).

25. van Wezel, J. et al. Effect of charge order on the plasmon dispersion in transition-metal dichalcogenides. *Phys. Rev. Lett.* **107**, 176404 (2011).

26. Husain, A. A. et al. Pines' demon observed as a 3d acoustic plasmon in Sr_2RuO_4. *Nature* **621**, 66–70 (2023).

27. Chamberland, B. Preparation and properties of $SrCrO_3$. *Solid State Commun.* **5**, 663–666 (1967).

28. Zhou, J.-S., Jin, C.-Q., Long, Y.-W., Yang, L.-X. & Goodenough, J. B. Anomalous electronic state in $CaCrO_3$ and $SrCrO_3$. *Phys. Rev. Lett.* **96**, 046408 (2006).

29. Arévalo-López, M. A. Electron energy loss spectroscopy in $ACrO_3$ (a = Ca, Sr and Pb) perovskites. *J. Phys. Condens. Matter* **20**, 505207 (2008).

30. Qian, Y., Wang, G., Li, Z., Jin, C. Q. & Fang, Z. The electronic structure of a weakly correlated antiferromagnetic metal, $SrCrO_3$: first-principles calculations. *N. J. Phys.* **13**, 053002 (2011).

31. Zhang, K. H. L. et al. Electronic and magnetic properties of epitaxial perovskite $SrCrO_3$(001). *J. Phys. Condens. Matter* **27**, 245605 (2015).

32. Carta, A., Panda, A. & Ederer, C. Emergence of a potential charge-disproportionated insulating state in $SrCrO_3$. *Phys. Rev. Res.* **6**, 023240 (2024).

33. Chmaissem, O. et al. Relationship between structural parameters and the néel temperature in $Sr_{1-x}Ca_xMnO_3$(0 < x < 1) and $Sr_{1-y}Ba_yMnO_3$(y < 0.2). *Phys. Rev. B* **64**, 134412 (2001).

34. Takeda, T. & Ohara, S. Magnetic structure of the cubic perovskite type $SrMnO_3$. *J. Phys. Soc. Jpn.* **37**, 275–275 (1974).

35. de Groot, F. M. F. et al. Oxygen 1s X-ray-absorption edges of transition-metal oxides. *Phys. Rev. B* **40**, 5715–5723 (1989).

36. Shinaoka, H., Troyer, M. & Werner, P. Accuracy of downfolding based on the constrained random-phase approximation. *Phys. Rev. B* **91**, 245156 (2015).

37. Wortmann, D. et al. The fleur project. http://www.flapw.de (2024).

38. Friedrich, C., Blügel, S. & Schindlmayr, A. Efficient implementation of the gw approximation within the all-electron FLAPW method. *Phys. Rev. B* **81**, 125102 (2010).

39. Pizzi, G. et al. Wannier90 as a community code: new features and applications. *J. Phys. Condens. Matter* **32**, 165902 (2020).

40. Werner, P., Comanac, A., de' Medici, L., Troyer, M. & Millis, A. J. Continuous-time solver for quantum impurity models. *Phys. Rev. Lett.* **97**, 076405 (2006).

41. Werner, P. & Millis, A. J. Dynamical screening in correlated electron materials. *Phys. Rev. Lett.* **104**, 146401 (2010).

42. Su, C.-P., Ruotsalainen, K., Nicolaou, A., Gatti, M. & Gloter, A. Plasmonic properties of $SrVO_3$ bulk and nanostructures. *Adv. Optical Mater.* **11**, 2202415 (2023).

Author contributions
R.M. ran the calculations and wrote the manuscript. F.P. assisted with running and debugging the self-consistency code. V.C. assisted with running and debugging the codes for input generation and self-consistency. P.W. supervised the work, proposed the project and helped with the writing of the manuscript. All authors have read and approved the manuscript.

Competing interests
The authors declare no competing interests.

Additional information
Supplementary information The online version contains supplementary material available at https://doi.org/10.1038/s41524-024-01376-6.

Correspondence and requests for materials should be addressed to Ruslan Mushkaev.

Reprints and permissions information is available at http://www.nature.com/reprints

Publisher's note Springer Nature remains neutral with regard to jurisdictional claims in published maps and institutional affiliations.